PROCEEDINGS, 47th Workshop on Geothermal Reservoir Engineering
Stanford University, Stanford, California, February 7-9, 2022
SGP-TR-223

Ambient Noise Imaging of the Lightning Dock Geothermal Field, New Mexico

Hao Zhang[1], Avinash Nayak[2], Joel Edwards[1], Verónica Rodríguez Tribaldos[2], Trenton Cladouhos[3]

[1]Zanskar Geothermal & Minerals, Inc. [2]Lawrence Berkeley National Laboratory [3]Cyrq Energy, Inc.

hao@zanskar.us

Keywords: ambient noise, geothermal reservoir, 3D shear-wave velocity model, Lightning Dock, large-N geophone array

ABSTRACT

From July 17-Aug. 19, 2020, we deployed and maintained a 1206 station array of 1C geophones over the footprint of the well-field at the Lightning Dock Geothermal (LDG) power plant in Hidalgo County, New Mexico. Such dense seismological data were collected for a variety of purposes, including to better characterize the shallow velocity structure. An initial *P*-wave velocity (*Vp*) model covering LDG was generated using reserse-VSP one-way travel times, sonic logs, well logs and gravity data (Edwards et al., 2021). However, such data only provided *Vp* velocity constraints and was mostly limited to the ray paths between sources within wells and array stations. Rayleigh waves can constrain S-wave (*Vs*) velocity structure, especially within shallow depths (less than 300 m), where large velocity changes can occur. Comparing *Vp* models with Vs models may yield insights into geothermal fluid upwelling and outflow over the shallow domain. To obtain the shear-wave velocity model, we applied ambient noise cross-correlation and surface-wave imaging methods to the vertical component data recorded across the station array. The raw data were processed following the workflow described by Bensen et al. (2007), including four phases: 1) data pre-processing including temporal and spectral normalization at individual stations, 2) cross-correlation and temporal stacking, 3) measurement of the dispersion curves using automatic frequency-time analysis and 4) quality control. Noise cross-correlations were stacked over nighttime hours to avoid the strongly inhomogeneous noise field during the daytime resulting from operations at the geothermal field. The resulting noise cross-correlations reveal empirical Rayleigh waves in the frequency range of ~1-4 Hz traveling across the geothermal field with well-defined average move-outs. An inversion for Rayleigh-wave group velocity dispersion curves for 75 reference stations was performed after manual quality checking. With the knowledge from results for the reference stations, we automatically extract group velocity dispersion curves for all the station pairs. The group velocity dispersion measurements are inverted for period-wise 2D group velocity maps. Finally, the 3D *Vs* model is inverted from the 2D group velocity maps over a range of periods. The 3D *Vp* and *Vs* models were then compared and were analyzed for their relationships to the geothermal reservoir and fluid migration.

1. INTRODUCTION

The Lightning Dock Geothermal field (LDG), New Mexico, hosts a blind geothermal reservoir broadly controlled by the N-S striking Animas Fault (Elston et al., 1983; Cuniff and Bowers, 2005; Crowell and Crowell, 2014). The thermal anomaly is 2.5 km long along the N-S direction and 1.5 km wide along the E-W direction (Elston et al., 1983). Although the shape of the thermal anomaly is known, the detailed structure of the reservoir, particularly flow paths away from wells and the well field, remains poorly understood. An improved characterization of these features could help increase the electricity productivity of the LDG field, currently hosting a 12 MWnet power plant.

Geothermal industry practitioners and academic researchers have long tried to adapt standard geophysical tools from other extractive industries (e.g., seismic reflection and microseismicity from oil and gas and electrical methods from groundwater research) to geothermal exploration with varied success (e.g., see seismic reflection imaging results at Blue Mountain, Brady's, Coso, Fallon FORGE, Utah FORGE, Rye Patch, Soda Lake and Walker Ranch; Melosh et al., 2010; Queen et al., 2016; Pullammanappallil et al., 2004; Blankenship et al., 2016; Miller, 2019; Gritto et al., 2002; Alterra Power Corp., 2012; Casteel et al., 2016). However, there have been significant method improvements since many of these past geophysical experiments, including the development of new seismology tools (the latter of which have been primarily built by academic groups, e.g., Shapiro and Campillo, 2004), that have obvious applications for de-risking geothermal resources but have yet to be applied at many operating or developing fields. One such tool is the use of the dispersive nature of surface waves to constrain the shear-wave velocity (Vs) structure of the shallow crust (referred to in academic literature as ambient seismic noise techniques).

Recent advancements in ambient seismic noise techniques, in combination with the acquisition of large-N sensing arrays for large-scale, high-resolution imaging and monitoring, have great potential to improve our ability to resolve the detailed velocity structure of geothermal systems. Ambient noise tomography has been broadly used to image Vs structure since the early 2000s (e.g., Shapiro et al., 2005). Originally, this technique was mainly used to study regional and continental scale Vs structure using low frequency (frequency $f < 0.2$ Hz) data (Ekström, 2014; Lin et al., 2008). However, more recent work has applied ambient noise tomography in <5 km x 5 km scale investigations using very dense, large-N nodal arrays and higher frequency ($f > 1$ Hz) data (Castellanos et al., 2020; Lin et al. 2013; Jia and Clayton, 2021).

Here, we applied ambient noise tomography to illuminate the 3D shear-wave velocity structure of the LDG using a large-N nodal array consisting of 1206 geophones., Noise cross-correlations between nodal sensors were calculated using nighttime data only, to avoid operational noise from the geothermal field. We performed frequency-time analysis on the noise cross-correlations to extract Rayleigh-wave group velocity dispersion curves, which were afterward inverted to generate 2D group velocity maps. Next, an inversion of 3D *Vs* structure was carried out using the group velocity maps. Finally, the derived 3D *Vs* models were compared with 3D *Vp* models generated from inversion of travel times from string shots conducted during the deployment of the large-N nodal array (Edwards et al., 2021).

2. DATA AND METHODOLOGY

The LDG array, consisting of 1206 geophones, was deployed for ~3 weeks and covered a ~3 km x 3 km area centered on the field production wells (Fig. 1). The array had an inner interstation spacing of ~75 m and an outer interstation spacing of ~100 m. Seismic measurements were made at a sample rate of 500 Hz using NuSeis NRU 1C seismic recording nodes (by Geophysical Technology Inc.), which house, power, digitize and record voltages from SunFull PS-10R geophones that have a natural frequency of 10 Hz. The deployment of the array aimed at imaging the detailed geothermal system of the LDG field.

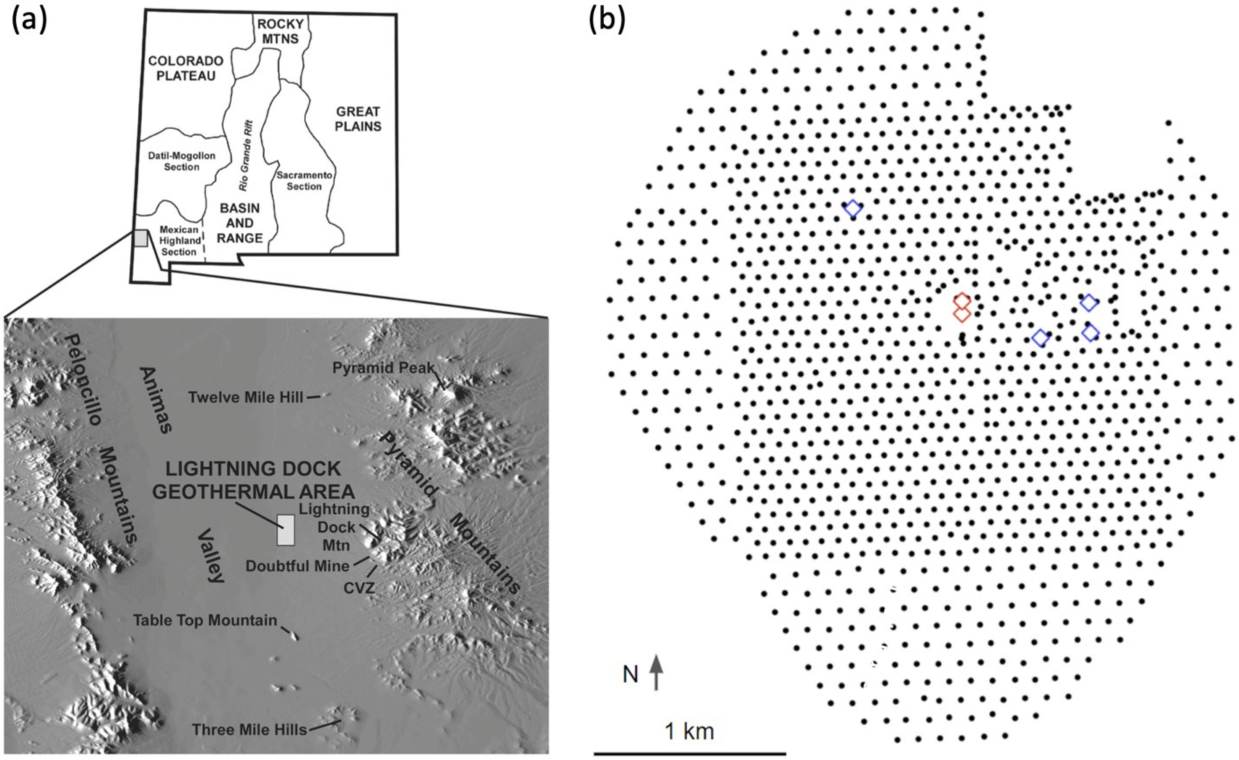

Figure 1. (a) Topographic location map of the Lightning Dock geothermal area (modified from Witcher, 2008). (b) Station distribution of the LDG nodal array. The black dots indicate the one-component geophones. The red and blue diamonds depict the production and injection wells, respectively.

2.1 Characterization of the Noise Wavefield

The cross-correlation of ambient seismic noise recorded at pairs of seismic sensors converges to the empirical Green's function of the medium between the two sensors acting as a pair of virtual source and virtual receiver (Shapiro & Campillo 2004). The concentration of ambient seismic noise sources across the Earth's surface results in the recovery of primarily surface waves that have been successfully used for surface-wave tomography at a range of spatial scales (Shapiro et al. 2005; Lehujeur et al. 2018; Planès et al. 2019). However, the degree to which the empirical Green's function can be recovered accurately depends on the uniformity of background noise distribution. Realistic non-uniform distribution of background noise sources and the presence of noise anomalies has been demonstrated to cause artifacts in the empirical Green's functions, in particular surface-wave precursors, that lead to errors in surface-wave dispersion estimates (Stehly et al. 2006, 2008).

We use the high spatial density and long duration of the data acquired to analyze the spatiotemporal variation of background noise amplitudes. We processed the seismic data in 3-hour segments. The raw data was decimated to 50 Hz and the median noise power spectral density in raw units (proportional to velocity) was calculated using the methodology of McNamara & Buland (2004). We used sliding time windows of 5 min, overlapping at 50% and the width of the frequency bands was 0.5 Octaves. Median noise power spectral density at all stations were interpolated over the study area to produce smooth maps for every 3-hour durations at frequencies from 1 Hz to 8 Hz. Figure 2 shows the distribution of noise amplitudes at 4 Hz for a 1-day period (2-3 August 2020). The noise amplitudes are high in the vicinity of the geothermal plant, near the center of the study area, during the day (local time 6 AM - 9 PM). The region with higher noise amplitudes is less pronounced at lower frequencies (1 Hz and 2 Hz) and more pronounced for longer durations of time at higher frequencies (8 Hz). We suspect this noise peak is caused by operations at the geothermal plant. The spatial noise peak became more pronounced from local time 2 PM, 5th August at nearly all times of the day when the plant resumed normal operations. To avoid the influence of the dominant noise source near the geothermal plant in the recovery of the empirical Green's functions and satisfy the assumption of uniform noise source distribution, we further restrict the noise cross-correlation analysis to night time (9 PM - 6 AM in local time) between 28 July and 4 August 2020. We observe a large amplitude contrast between northern and central sections of the array across an east-west trending line (Highway C096; "Geothermal Road"). This is possibly caused by a difference in coupling with the ground due to a difference in the packaging of Sunfill PS-10R geophone sensors between two different generations of nodes deployed in these two sections of the array (Nuseis NRU EL1 nodes across most of the array and NRU N1 nodes only in the northwest section, north of Geothermal Road).

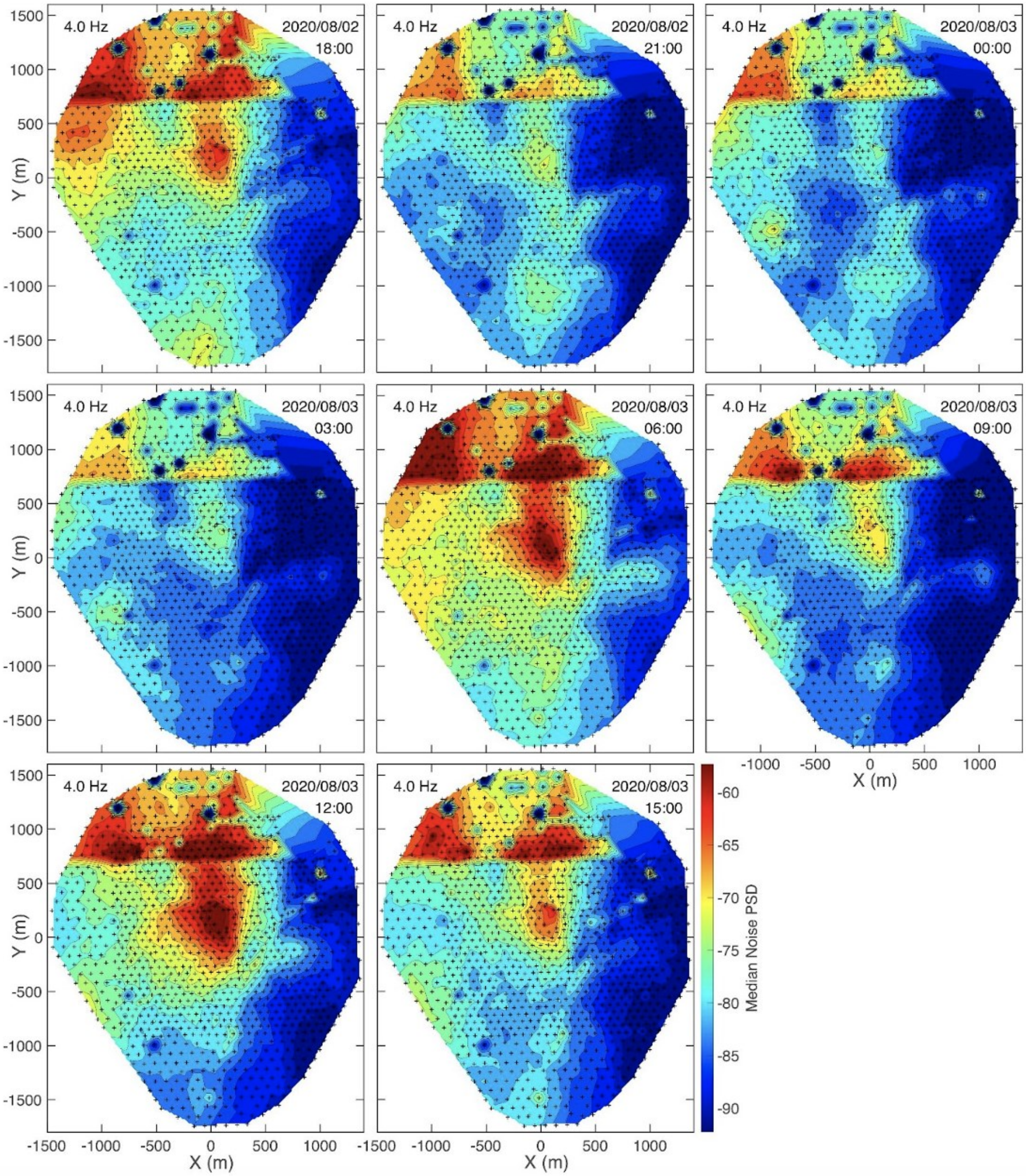

Figure 2. Noise power spectral density at 4 Hz over the geothermal field for 3-hour time windows on 2-3 August 2020. The local time is indicated in the top right corner. The color scale is the same for all the plots (shown on the last plot). Station locations are indicated by '+' marks.

2.2 Data processing for noise cross-correlations

Our methodology is approximately derived from Bensen et al. (2007). For each station, we assemble 3-hour segments of waveform data, detrend and decimate them to 50 Hz. The data were not corrected for instrument response because all sensors were the same model. For temporal normalization, we calculate smooth amplitude envelopes in multiple passbands: 0.2–1 Hz, 1–10 Hz and 0.2–10 Hz, normalized by the mean absolute amplitude for the entire duration. For each station, we make a composite amplitude ratio envelope time-series, choosing the largest value of amplitude ratio from all passbands for each time sample. The temporal normalization factors are set to a scaled reciprocal of the composite amplitude ratio if they exceed a particular threshold, otherwise they are set to 1. This procedure reduces amplitudes of data at instances of anomalously large amplitudes at a range of possible frequencies, while leaving much of the waveforms unchanged. 2.5-min-long time windows, overlapping by 75%, are Fourier transformed to the frequency domain for spectral normalization and cross-correlation. A band limiting taper is applied outside 0.2-10 Hz during spectral normalization. Ultimately, we did not recover any useful coherent energy in the noise cross-correlations below ~0.9 Hz and above ~5 Hz. We discard time windows with large amplitudes over extended durations. The cross-correlations for all windows during nighttime (9 PM - 6 AM local time) between 28 July and 04 August are stacked to form a final reference stack.

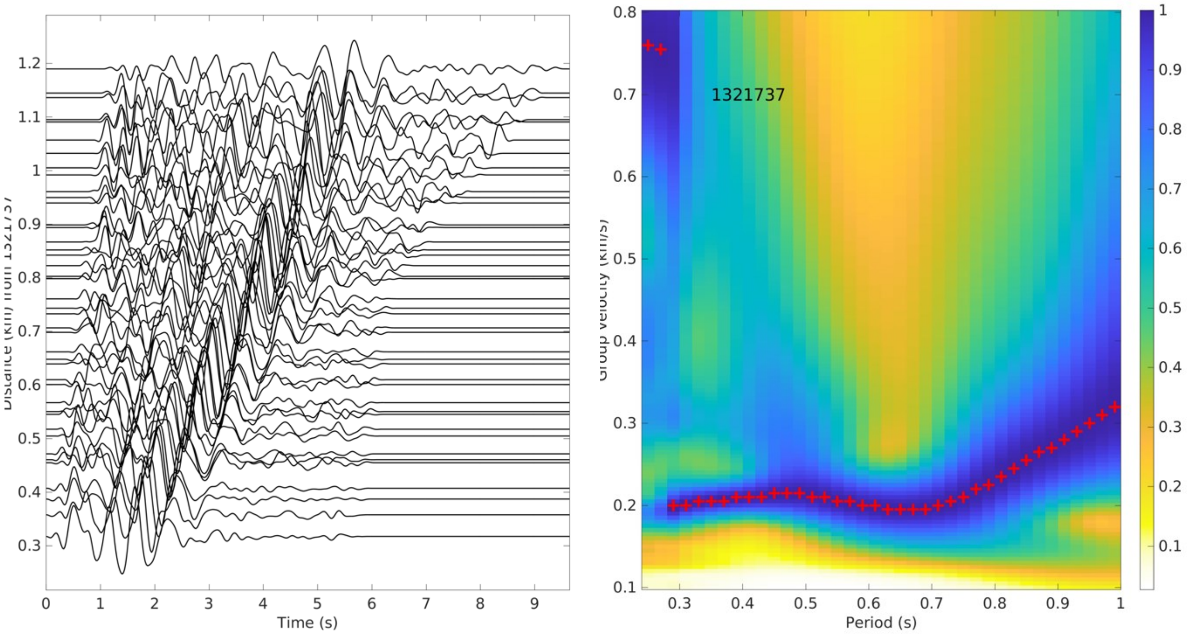

Figure 3. (a) Vertical-component noise cross-correlations filtered in the passband 0.8-4 Hz for station pairs with station 1321737 at an azimuthal range of 135°N-180°N. (b) Average group velocity dispersion image for the noise cross-correlations shown in (a). The red + marks are the picked group velocity dispersion measurements.

For quality control, we manually review noise cross-correlations in 45° azimuth bins in the interstation distance range 0.3-1.2 km for 75 selected reference stations semi-uniformly distributed over the study area at ~0.3 km spacing Figure 3 shows an example for station 1321737 located in the south-eastern section of the geothermal field. The noise cross-correlations are composed of dispersive, coherent Rayleigh waves with a consistent moveout (Figure 3a). The waveforms are windowed around the ballistic Rayleigh wave arrivals and filtered in narrow frequency passbands (Herrmann 1973). The envelope of the filtered waveforms at different frequencies constitutes a group velocity dispersion image. Following the methodology of Campillo et al. (1996), in order to improve the accuracy and precision of the group velocity measurements, we linearly stack the dispersion images of the individual noise cross-correlations to estimate an average group velocity dispersion image, representative of the region in a specific azimuth and distance range with respect to each reference station (Figure 3b). Stacking multiple dispersion images suppresses noise, thereby leading to a well-defined peak in the averaged dispersion image and improved group velocity dispersion estimates. After quality control, we invert the average group dispersion curves for average 1D *Vs* profiles over the study area using the surf96 method (Herrmann, 2013). The 1D velocity model is parameterized as a stack of ten flat layers of constant velocity and 25 m thickness. Group velocity dispersion measurements at these periods (~0.25 s to ~0.9 s) are primarily sensitive to the top ~200 m. Group velocity at each period was weighted by the corresponding amplitude at the peak in the stacked dispersion image. In the inversion, we impose damping and smoothing on model perturbations for all layers with the halfspace velocities remaining fixed and slightly greater damping for deeper layers. Due to the limited frequency range of the dispersion measurements, we force the velocity gradient to be non-negative. We assumed a constant *Vp*/*Vs* ratio of 1.9 as surface-wave dispersion has negligible sensitivity to *Vp* at these periods. We assume a simple Vs model with velocities increasing from 0.19 km/s at the surface to 0.87 km/s at 250 m depth based on visual inspection of the dispersion curves as the initial model. Figure 4a shows the observed group velocity dispersion curve along with the predicted dispersion curves for the initial and the inverted models. The results show excellent agreement between the observed and predicted group velocity dispersion curves for a minor change in the velocity model (Figure 4b). The average Vs model inverted for all reference stations over all azimuthal bins with a well-defined ballistic surface-wave (Figure 5) is further used as a reference to measure dispersion curves for all noise cross-correlation waveforms at distance > 0.3 km using Automated Frequency Time Analysis (AFTAN) (Bensen et al. 2007, Lin et al. 2008). We assume a phase velocity range of 0.13 to 0.8 km/s at frequencies 1 to 8 Hz. We impose a minimum interstation distance of 0.3 km and a minimum station separation threshold of 2 times the wavelength. We select group velocity measurements with signal-to-noise ratio (SNR) > 2 for surface-wave for tomography.

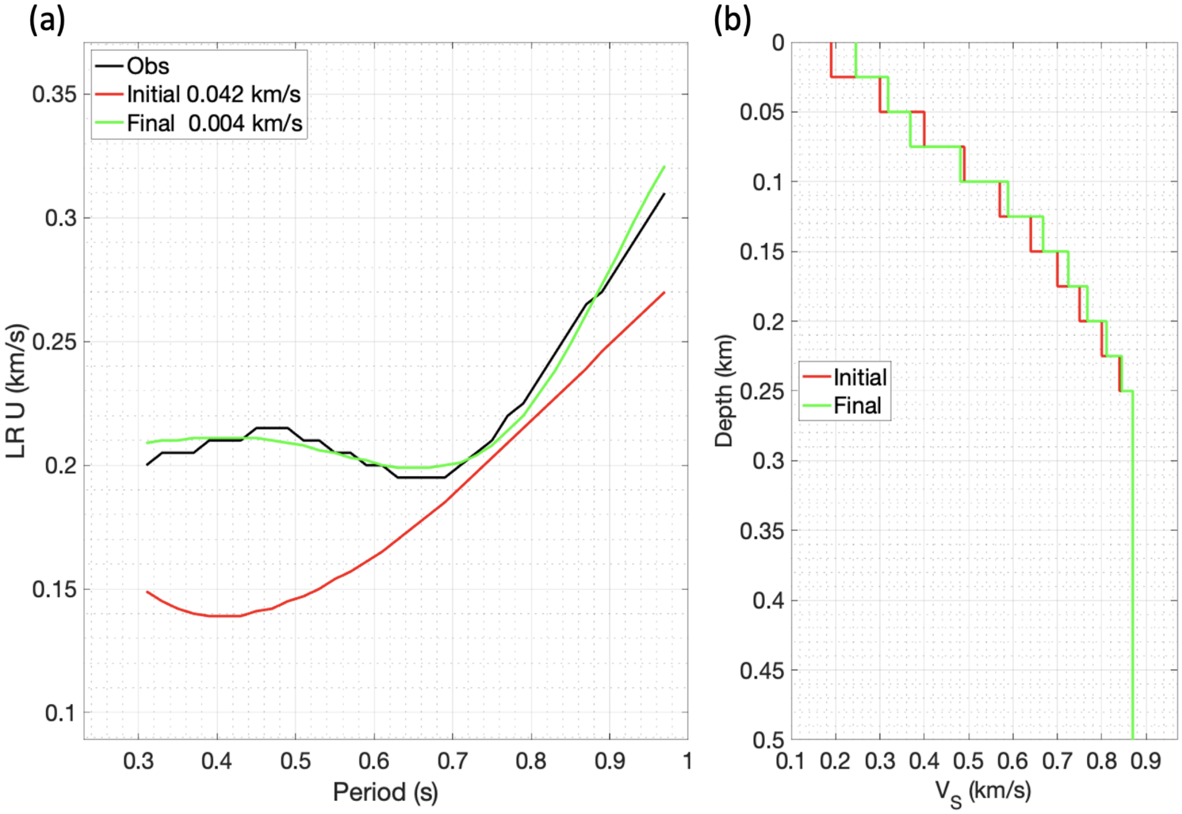

Figure 4. (a) Black line is the observed average group velocity dispersion curve shown in Figure 3b. Red and green curves are synthetic dispersion curves for the initial and the final inverted *Vs* models shown in (b). The misfits for the initial and final model are indicated on the top left corner of (a).

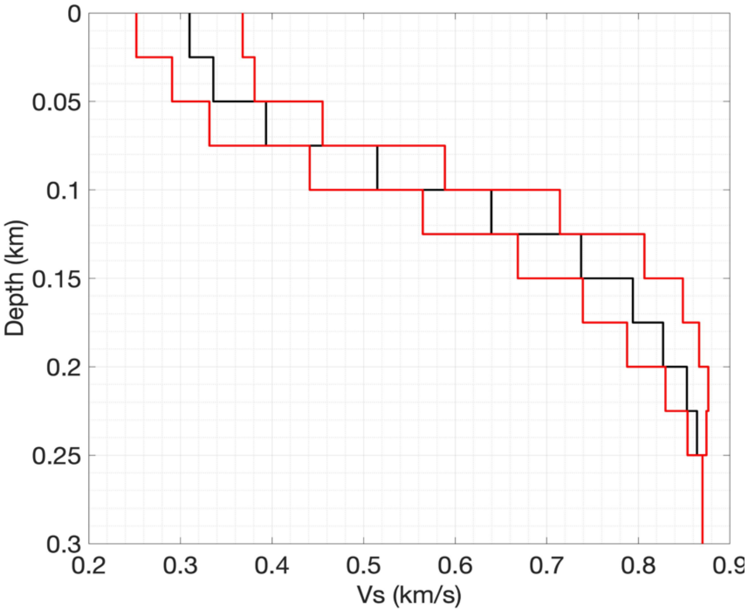

Figure 5. Black line is the median of 1D *Vs* profiles inverted from the average group velocity dispersion curves at the reference stations. The red lines indicate +/-1 standard deviation.

We invert the Rayleigh-wave group velocity measurements at each period from ~0.22 s (~4.6 Hz) to ~0.8 s (~1.25 Hz) for 2D group-velocity maps at grid spacing ~0.002° (~200 m) using the 2D fast marching surface-wave tomography method (Rawlinson and Sambridge, 2004). We tested a range of smoothing and damping parameters for the tomographic inversion of the 2D maps as shown in Figure 6. The optimum values were selected after examining the final maps, the minimum and maximum velocities and the final misfit. Generally, we observe a ~30-60% decrease in weighted root-mean-square of the residuals for the inverted model with respect to that for the initial uniform model with value assumed to be the average of all group velocity measurements at that period. For each XY (latitude–longitude) point in the 2D maps, we inverted the Rayleigh-wave group-velocity values at all periods for a vertical 1D *Vs* profile using the procedure described earlier. However, a maximum of 40 m/s velocity inversion is allowed between two consecutive layers. Group velocity at each period, at each node, was weighted by the derivative weighted sum (DWS) at that node in the group-velocity map at that period. Thereafter, we assembled a 3D Vs model from the initial set of 1D *Vs* models.

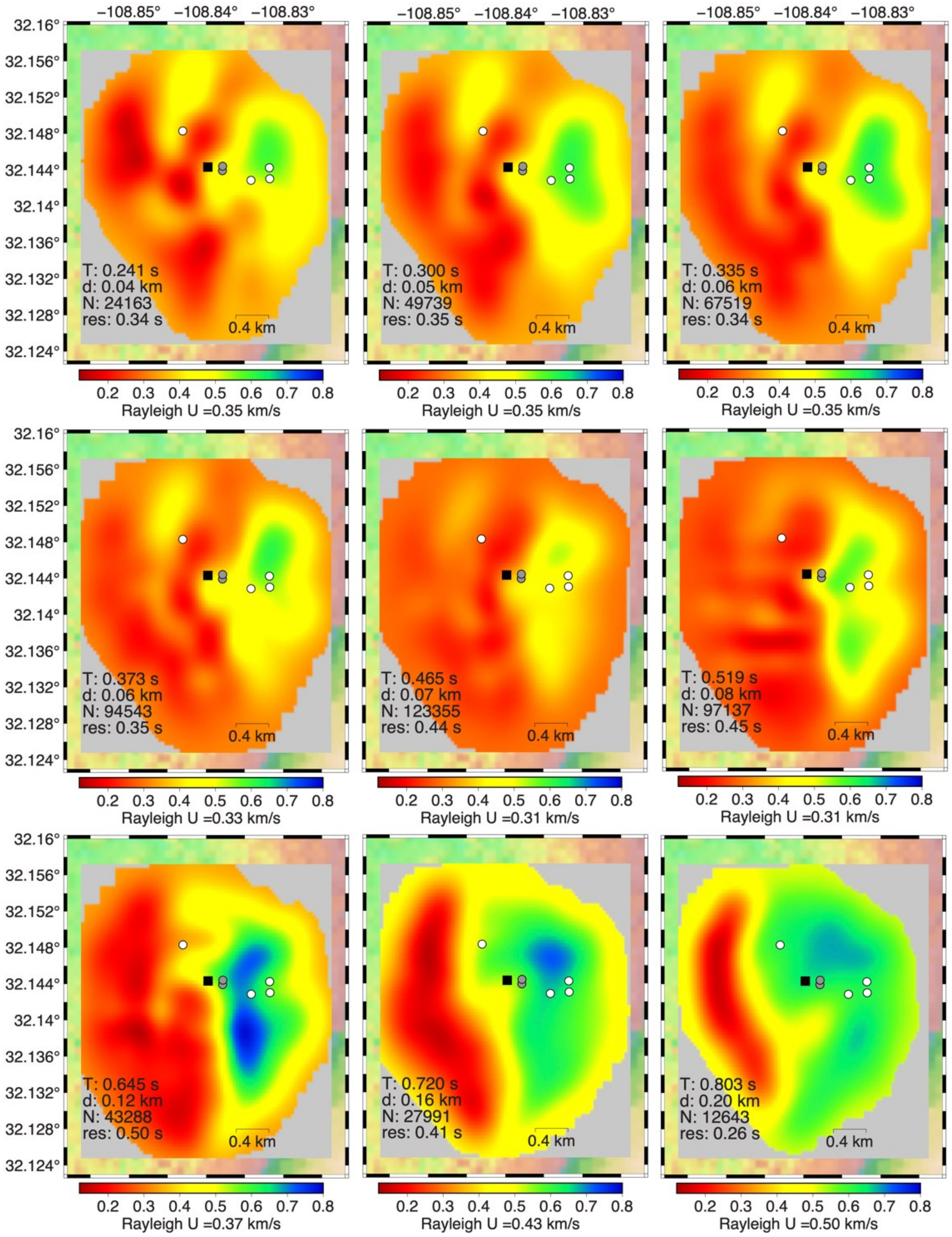

Figure 6. Group velocity maps for different periods. The color bar indicates the Rayleigh wave group velocity: reddish color depicts lower group velocity, while blueish color represents the higher group velocity. The time period (T), the maximum depth sensitivity for this period (d ~ half the average wavelength), number of measurements at this period (N) and root-mean-square value of residuals (res) are indicated at the lower left corner of each plot. Areas with poor resolution are masked in gray (DWS < 10). White circles: injection wells, gray circles: production wells, black square: geothermal plant.

3. RESULTS

The 3D *Vs* models (down to ~200 m) derived from the surface wave group dispersion curves (Figure 7) show a high velocity unit to the east and a low- velocity unit to the west, with slightly varying shapes with depth. We interpret these high and low velocity units as the basement and basin sediment infill, respectively. The major orientation of both units is N-striking which agrees with the geologic and well field data (Crowell and Crowell, 2014). The linear feature separating the basement on the east side from the sediments on the west side is interpreted to be a fault that may be part of the Animas Valley fault zone. The interpreted location of the fault moves towards the west as depth increases, indicating the fault dips to the west. Moreover, the orientation of the northern part of the fault changes from NNE-striking near the surface and N-striking at greater depths. Another intriguing feature is a consistent low *Vs* anomaly from 87 m depth to 212 m depth close to the center of the study region, near where the two production wells are located (Figure 1). Future work will include checkerboard tests for confirming this small feature and the structures at the edges of all the *Vs* maps are not trustable because of lack of ray crossing of stations.

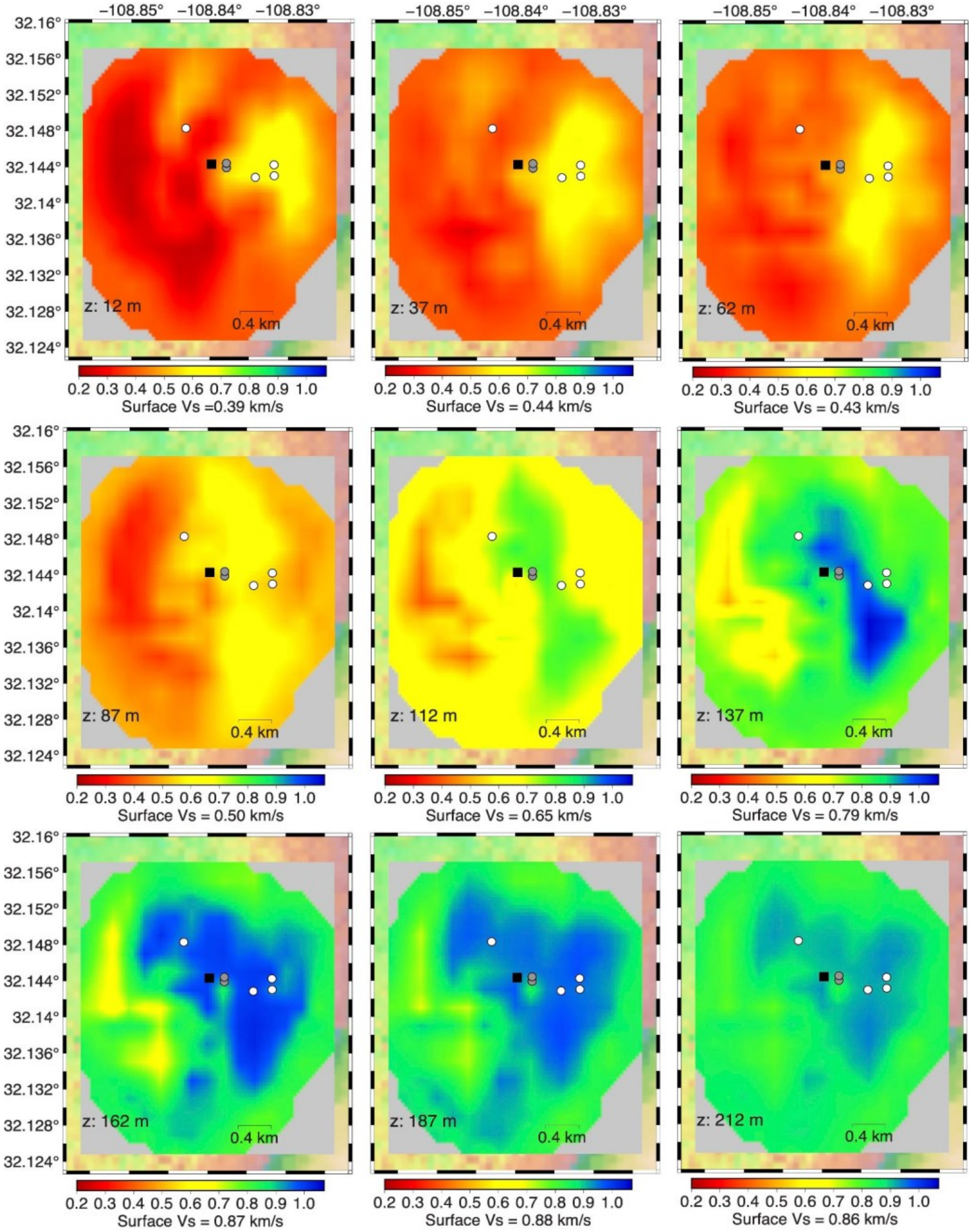

Figure 7. 3D Vs Model at depths 12 m, 37m, 62 m, 87m, 112 m, 137 m, 162 m, 187 m, and 212 m (indicated at the lower left corner). The color bar indicates the shear-wave velocity: reddish color depicts lower *Vs*, while blueish color represents the higher *Vs*. Areas with poor resolution are masked in gray. White circles: injection wells, gray circles: production wells, black square: geothermal plant.

4. DISCUSSION

Ambient noise tomography combined with large-N nodal array data provides a powerful way to constrain the Vs structure at geothermal fields. For the LDG field, the modeled 3D Vs structure not only parallels the horst and graben geological setting, but its structure is like the modeled 3D P-wave velocity structure (Figure 8). However, the location of the fault in the *Vp* model is to the east of its location in the Vs model. This could be caused by sampling density or raypath differences between the string shot sourced p-waves and ambient noise Rayleigh waves, sparser grid cell sizes in the *Vp* model or to different depth sensitivities. Regardless, the position of the fault, as highlighted by both *Vs* and *Vp* models, is located ~1 kilometer west of where the Animas Valley fault zone ruptures the surface (USGS, 2022), suggesting the fault zone may be wider than earlier interpretations and may have fault strands that host significant offsets but that are buried (have no surface expressions).

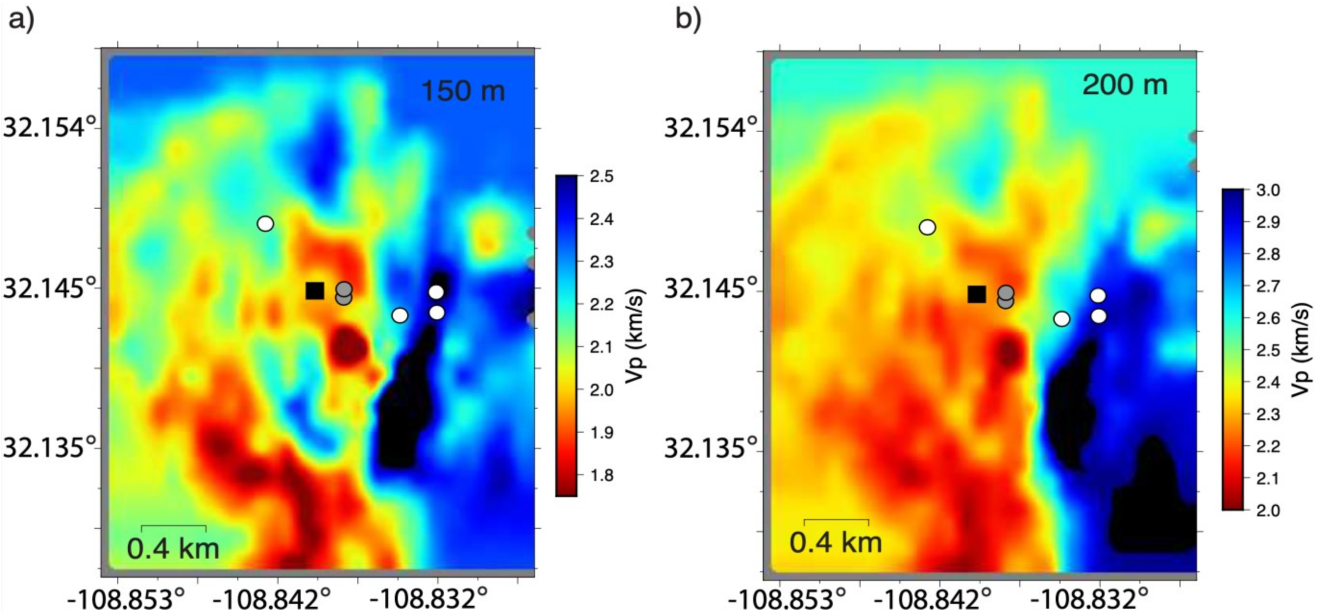

Figure 8. *P*-wave velocity models at depths of (a) ~150 m and (b) ~200 m (Edwards et al., 2021). The color bar indicates the *P*-wave velocity: reddish color depicts lower *Vp*, while blueish color represents the higher *Vp*. White circles: injection wells, gray circles: production wells, black square: geothermal plant.

In the near future, we plan to produce *Vs* models inverted by fitting phase dispersion curves, which can generate higher resolution models than those constrained by group velocity dispersion curves. Having complementary *Vs* models obtained from phase and group velocity maps will improve their interpretability in the context of constraining structures associated with the geothermal resource. Finally, despite the careful selection of data used in the analysis (only night hours during a power plant shutdown period), we still observed some contamination in the noise cross-correlation waveforms. Advanced processing methodologies such as double beamforming can be used to minimize the errors caused by such artifacts (Roux et al., 2016).

5. CONCLUSIONS

To better image the detailed structure of the geothermal reservoir at the Lightning Dock Geothermal Field in Hidalgo County, New Mexico, we utilized the ambient seismic noise signals recorded by a dense, large-N array dataset collected during 2020. We used such ambient seismic noise data to generate cross-correlations between stations, then to extract Rayleigh wave group dispersion curves, and to finally invert for the 3D *Vs* model. The *Vs* model clearly shows a known west-dipping fault separating the basement to the east from the sediments to the west. Additionally, a low *Vs* anomaly near the production wells is observed over a ~125 meters depth interval. Our findings are relevant to understanding the structure of the geothermal field and highlight the importance of, and opportunities for, further research and development of passive seismic methods for quantitative characterization of geothermal reservoirs.

ACKNOWLEDGEMENTS

We thank Cryq Energy for funding and collaborating with us in acquiring the large-N dataset and for the permission to present this work.

REFERENCES

Alterra Power Corp., 2012, A 3D-3C Reflection Seismic Survey and Data Integration to Identify the Seismic Response of Fractures and Permeable Zones over a Known Geothermal Resource: Soda Lake, Churchill County, Nevada: DE-EE0002832 final report, Unpublished Final Report to U. S. Dept. of Energy, 46 p.

Blankenship, D., Akerley, J., Blake, K., Calvin, W., Faulds, J.E.,Glen, J.M.G., Hickman, S., Hinz, N., Kaven, O., Lazaro, M.,Meade, D., Kennedy, B.M., Phelps, G., Sabin, A., Schoenball,M., Siler, D.L., Robertson-Tait, A., and Williams, C., 2016. Frontier Observatory for Research in Geothermal Energy—Phase 1 topical report, Fallon, NV: Sandia National Laboratories Report, SAND2016-8929, 311 p.

Campillo, M., Singh, S. K., Shapiro, N., Pacheco, J & Hemnann, R. B., 1996. Crustal structure south of the Mexican volcanic belt, based on group velocity dispersion, Geof. Int., 35(4), 361–370.

Casteel, J., Pullammanappallil, S. and Mellors, R.J., 2016. Estimating subsurface permeability with 3D seismic attributes: A neural net approach: Proceedings, 41st Workshop on Geothermal Reservoir Engineering Stanford University.

Castellanos, J. C., Clayton, R. W., and Juarez, A., 2020. Using a Time-based Subarray Method to Extract and Invert Noise-derived Body Waves at Long Beach, California. Journal of Geophysical Research: Solid Earth, 125(5), e2019JB018855. https://doi.org/10.1029/2019jb018855

Crowell, J., and Crowell, A., 2014, The History of Lightning Dock KGRA: Identifying a Blind Geothermal Resource: GRC Transactions, v. 38.

Cunniff, R. A., and Bowers, R. L., 1988, Temperature, water-chemistry, and litho- logical data for the Lightning Dock Known Geothermal Resources Area, Animas Valley, New Mexico, in Icerman, L., and Parker, S. K., eds., New Mexico Statewide Geothermal Program: New Mexico Research and Devel- opment Institute, p. 3-1 to 3-37.

Edwards, J., Hoiland, C., Fleure, T., Sicking, C., McLain, B., Vermilye, J., Twitter, J., Tanner, N., and Cladouhos, T., 2021, Seismic imaging of resonating fracture networks at the Lightning Dock Geothermal field, Hidalgo County, New Mexico: Geothermal Resources Transactions, Vol. 45.

Ekström, G., 2014. Love and Rayleigh phase-velocity maps, 5–40 s, of the western and central USA from USArray data. Earth and Planetary Science Letters, 402, 42–49. https://doi.org/10.1016/j.epsl.2013.11.022

Elston, W. E., Deal, E. G., and Logsdon, M. J., 1983, Geology and geothermal waters of Lightning Dock region, Animas Valley and Pyramid Mountains, Hidalgo County, New Mexico: New Mexico Bureau of Mines and Mineral Resources, Circular no.177, 44 pp.

Gritto, R., Daley, T.M., and Majer, E.L., 2002. Integrated Seismic Studies at the Rye Patch Geothermal Reservoir: Geothermal Resources Council.

Herrmann, R.B., 1973. Some aspects of band-pass filtering of surface waves, Bull. seism. Soc. Am., 63(2), 663–671.

Herrmann, R. B. (2013). Computer programs in seismology: An evolving tool for instruction and research, Seismol. Res. Lett. 84, no. 6, 1081–1088, doi: 10.1785/0220110096.

Jia, Z., and Clayton, R. W., 2021. Determination of near surface shear-wave velocities in the central Los Angeles Basin with dense arrays. Journal of Geophysical Research: Solid Earth, 126, e2020JB021369. https://doi. org/10.1029/2020JB021369

Lehujeur, M., Vergne, J., Schmittbuhl, J., Zigone, D., Le Chenadec, A., & EstOF Team (2018). Reservoir imaging using ambient noise correlation from a dense seismic network. Journal of Geophysical Research: Solid Earth, 123, 6671–6686. https://doi.org/10.1029/2018JB015440

Lin, F.-C., Moschetti, M.P. & Ritzwoller, M.H., 2008. Surface wave tomography of the western United States from ambient seismic noise: Rayleigh and Love wave phase velocity maps, Geophys. J. Int., 173, 281–298.

Lin, F.-C., Li, D., Clayton, R.W. & Hollis, D., 2013. High-resolution 3D shallow crustal structure in Long Beach, California: application of am- bient noise tomography on a dense seismic array, Geophysics, 78(4), Q45–Q56.

McNamara, D. E., & Buland, R. P., 2004. Ambient noise levels in the continental United States. Bulletin of the Seismological Society of America, 94(4), 1517–1527. https://doi.org/10.1785/012003001

Melosh, G., Cumming, W., Casteel, J., Niggemann, K., and Fairbank, B., 2010. Seismic Reflection Data and Conceptual Models for Geothermal Development in Nevada: In Proceedings of the World Geothermal Congress, Bali, Indonesia, 25–29 April 2010; pp. 25–29.

Miller, J., 2019, 2018-2019 reprocessing of the 2D and 3D multichannel seismic surveys at the FORGE Utah EGS Laboratory, Subtask 2C.4.4.

Planès T, Obermann A, Antunes V, Lupi M., 2019. Ambient-noise tomography of the Greater Geneva Basin in a geothermal exploration context. Geophysical Journal International 220(1): 370–383.

Pullammanappallil, S., Honjas, W., Unruh, J., and Monastero, F., 2004. Active and Passive Seismic Investigations in the Coso Geothermal Field, Eastern California: Geothermal Resources Council Transactions, Vol. 28.

Queen, J.H., Daley, T.M., Majer, E.L., Nihei, K.T., and Siler, D.L., 2016, Surface Reflection Seismic and Vertical Seismic Profile at Brady's Hot Springs, NV, USA: Proceedings, 41st Workshop on Geothermal Reservoir Engineering, Stanford University.

Rawlinson, N., and M. Sambridge, 2004. Wave front evolution in strongly heterogeneous layered media using the fast-marching method, Geophys. J. Int. 156, 631–647, doi: 10.1111/j.1365-246X.2004.02153.x.

Roux, P., Moreau, L., Lecointre, A., Hillers, G., Campillo, M., Ben-Zion, Y., Zigone, D. & Vernon, F., 2016. A methodological approach towards high-resolution surface wave imaging of the san jacinto fault zone using ambient-noise recordings at a spatially dense array, Geophys. J. Int., 206, 980–992.

Shapiro, N.M. & Campillo, M., 2004. Emergence of broadband Rayleigh waves from correlations of the ambient seismic noise, Geophys. Res. Lett., 31, L07614, doi:10.1029/2004GL019491.

Shapiro, N.M., Campillo, M., Stehly, L. & Ritzwoller, M.H., 2005. High resolution surface wave tomography from ambient seismic noise, Science, 307, 1615–1618.

Stehly, L., Campillo, M. & Shapiro, N.M., 2006. A study of the seismic noise from its long-range correlation properties, J. geophys. Res., 111, B10306, doi:10.1029/2005JB004237.

Stehly, L., Campillo, M., Froment, B. & Weaver, R.L., 2008. Reconstructing Green’s function by correlation of the coda of the correlation (C3) of ambient seismic noise, J. geophys. Res., 113, B11306, doi:10.1029/2008JB005693.

U.S. Geological Survey and New Mexico Bureau of Mines and Mineral Resources, Quaternary fault and fold database for the United States, accessed January 23, 2022, at: https://www.usgs.gov/natural-hazards/earthquake-hazards/faults.